All-optical formation of coherent dark states of silicon-vacancy spins in diamond

Benjamin Pingault,[1,*] Jonas N. Becker,[2,*] Carsten H. H. Schulte,[1] Carsten Arend,[2] Christian Hepp,[1] Tillmann Godde,[3] Alexander I. Tartakovskii,[3] Matthew Markham,[4] Christoph Becher,[2,†] and Mete Atatüre[1,†]

[1] *Cavendish Laboratory, University of Cambridge, JJ Thomson Ave, Cambridge CB3 0HE, UK*
[2] *Fachrichtung 7.2 (Experimentalphysik), Universität des Saarlandes, Campus E2.6, 66123 Saarbrücken, Germany*
[3] *Department of Physics and Astronomy, University of Sheffield, Sheffield S3 7RH, UK*
[4] *Element Six Ltd., Global Innovation Centre, Fermi Avenue, Harwell Oxford, Didcot, OX11 0QR, UK*

(Dated: October 31, 2014)

Spin impurities in diamond can be versatile tools for a wide range of solid-state-based quantum technologies, but finding spin impurities which offer sufficient quality in both photonic and spin properties remains a challenge for this pursuit. The silicon-vacancy center has recently attracted a lot of interest due to its spin-accessible optical transitions and the quality of its optical spectrum. Complementing these properties, spin coherence is essential for the suitability of this center as a spin-photon quantum interface. Here, we report all-optical generation of coherent superpositions of spin states in the ground state of a negatively charged silicon-vacancy center using coherent population trapping. Our measurements reveal a characteristic spin coherence time, T_2^*, exceeding 45 nanoseconds at 4 K. We further investigate the role of phonon-mediated coupling between orbital states as a source of irreversible decoherence. Our results indicate the feasibility of all-optical coherent control of silicon-vacancy spins using ultrafast laser pulses.

PACS numbers: 42.50.-p, 42.50.Gy, 61.72.jn, 81.95.ug

Confined impurity spins in spin-free materials such as diamond and silicon offer a multitude of opportunities ranging from fundamental studies of engineered mesoscopic spin system dynamics to potential applications emerging from quantum control. A fundamental advantage of diamond-based impurities, known as color centers, is that they can be optically active in the conveniently detectable visible to near infrared region of the spectrum [1, 2]. Of these, the nitrogen-vacancy center (NV) remains the most studied one [3–6]. Sharing its desirable and undesirable properties alike, a handful of other impurities have recently been investigated [7]. These investigations reveal, for the NV center, the presence of crystal-field splitting in the ground state manifold allowing for feasible microwave control [8–11]. However, the unfavorable, but dominant, emission into phonon sidebands also occurs in these centers. Contemporary research efforts focus on two parallel approaches: Amplifying the zero-phonon emission by coupling selectively to an optical mode of a cavity [7, 12–15] and investigating alternative color centers with sufficiently small phonon sideband contribution to the full optical spectrum [7, 13].

The negatively charged silicon-vacancy (SiV^-) center is a particularly interesting justification to pursue the latter of the two approaches: The optical transitions coupling the excited and the ground state manifolds are predominantly into the zero-phonon line [16], which can be further enhanced by making use of the ongoing progress in diamond-based optical cavity nanostructures [17]. Also, the impressively small variation in the emission spectrum among multiple SiV^- centers in a clean diamond matrix [18, 19] deems them desirable for coupling multiple spins via a common photonic mode with a view to designing a distributed quantum network [20, 21]. In parallel, recent demonstrations of the direct optical access to the spin degrees of freedom of single SiV^- centers [22] offer the exciting possibility to employ full quantum control relying only on optical fields [23, 24], which can bring the speed-up advantage of optics over control techniques in the microwave regime. However, there are a number of open questions that need to be answered before such steps forward can be taken. Arguably, the most pressing challenge is to determine the coherence time of the SiV^- spin in the ground state in the presence of the potentially detrimental coexistence of the spin and orbital degrees of freedom. In this Letter, we achieve coherent population trapping (CPT) between Zeeman-split states as a means to generate a coherent superposition, i.e. coherent dark state, of a single SiV^- center spin. We report a spin coherence time (T_2^*) lower bound of 45 ns - more than an order of magnitude longer than the optical transition timescale [19, 26]. We first identify the operational conditions for generating the Λ system required for CPT by controlling the angle of the applied magnetic field. We further investigate the role of phonons as a source of decoherence within the ground state by tuning the spin states across an avoided crossing, where spin orthogonality is relaxed.

We investigate two samples, an electronic grade (001)-oriented CVD diamond used for magnetic-field orientation measurements and a (111)-oriented type IIa high-pressure-high-temperature (HPHT) diamond used for spin coherence measurements. SiV^- centers are generated by ^{28}Si implantation followed by thermal annealing. To enhance the optical excitation and collection efficiencies, arrays of solid immersion lenses (SILs) are fabricated on the surfaces of both samples using a focused ion beam (FIB) (for further details, see [27]). All our experiments are carried out at 4 K.

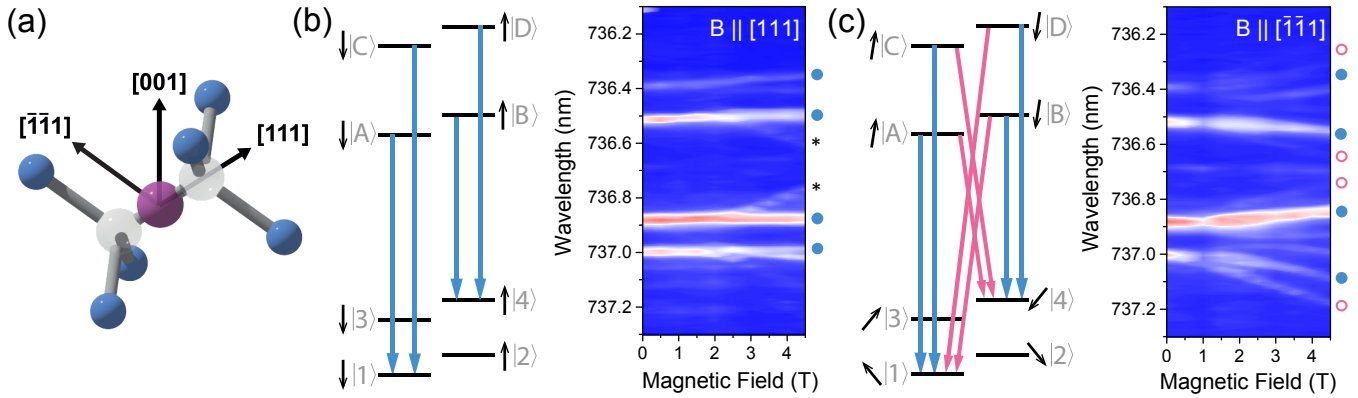

FIG. 1: (Color online) (a) Atomic structure of the SiV$^-$ color center, consisting of a Si impurity (purple) situated on an interstitial position along the [111] bond axis and surrounded by a split-vacancy (light grey) and the next-neighbor carbon atoms (blue). (b, left) Resulting energy levels and spin projections for magnetic fields applied along [111]. The level scheme shown here is simplified (a detailed scheme can be found in [27]). Optical transitions (blue arrows) are allowed between levels of the same spin state and the most visible ones are marked by blue dots in the magnetic field-dependent non-resonant fluorescence spectrum at 4 K (excitation at 660 nm) (b, right). Applying the magnetic field along the [$\bar{1}\bar{1}$1] direction on the same SiV$^-$ center, transverse field components lead to a finite spin overlap for all ground and excited states (c, left), resulting in additional optical transitions (pink arrows), observed in the field dependent spectrum (c, right). The spin labels refer to a Bloch vector representation, as explained in [27]. Energy levels are labelled according to Ref. [29], with labels ranging from 1 to 4 in the ground state, and from A to D in the excited state.

An SiV$^-$ center is formed by a substitutional silicon atom and a vacancy replacing two neighboring carbon atoms in the diamond matrix along the ⟨111⟩ axes. The silicon atom relaxes to the interstitial lattice site to form an inversion-symmetric split-vacancy structure [see Fig. 1(a)] [28]. The spin-orbit coupling dictates an inherent quantization axis for the spin degree of freedom aligned with the SiV$^-$ symmetry axis in both the ground and the excited state manifolds [29]. Figure 1(b) displays the fluorescence spectrum from a single SiV$^-$ center in the (001) sample under non-resonant excitation with a magnetic field applied along this inherent [111] quantization axis. The dominant optical transitions (four of which marked by blue filled circles) conserve the spin state, as illustrated in the accompanying energy level scheme. Weaker transitions, identified by asterisks, arise due to a slight mismatch between the symmetry axis and the direction of the applied magnetic field. This serves to reveal the importance of the magnetic field orientation for optical transition rules in the SiV$^-$ center level scheme.

A magnetic field, applied at a finite angle to the [111] direction, constitutes an external quantization axis which competes with the SiV$^-$ center's internal counterpart. The ground and excited state manifolds experience different strength of spin-orbit interaction [29]. Consequently, this configuration gives rise to different effective quantization axes between the two manifolds. The net angle between these resultant quantization axes, in turn, determines the optical selection rules for the fluorescence spectrum. Figure 1(c) presents the same measurement as Fig. 1(b), but for a [$\bar{1}\bar{1}$1]-oriented magnetic field. The spin selectivity of the optical transitions no longer holds and new optical transitions arise as the strength of the magnetic field increases. Four of these additional transitions are indicated by pink open circles and pink arrows. In summary, the fully aligned magnetic field case [Fig. 1(b)] yields cycling transitions, whereas a magnetic field at an angle allows for typical Λ schemes, where two orthogonal spin ground states can have finite transition matrix elements to the same excited state. This provides the desired configuration for all-optical manipulation of the SiV$^-$ spin via this shared excited state.

Figure 2 illustrates the detection strategy and characterization of the SiV$^-$ center used for coherent population trapping. We start by identifying a bright SiV$^-$ center within the SIL array of the (111) sample. Superimposed images of electron and fluorescence microscopy scans for the same area of the sample, as shown in Fig. 2(a), demonstrate an example of enhanced SiV$^-$ fluorescence under one of the SILs. Figure 2(b) shows the detection concept for all single- and multi-laser resonant excitation experiments, where the signal is obtained by measuring the integrated fluorescence from the transitions in the shaded area as a function of the excitation laser frequency. Non-radiative decay into the lower orbital branch of the excited state followed by fluorescence allows us to monitor excited-state population directly with no residual laser contribution [22]. In order to allow Λ schemes, the angle between the external magnetic field and the SiV$^-$ center axis is set to 109.4°, i.e. the angle between [$\bar{1}\bar{1}$1] and [111] directions [see Fig. 1(a)]. Pulsed intensity-correlation measurements performed on the selected SIL suggest the presence of two individual SiV$^-$ centers with strong spatial and spectral overlap [27].

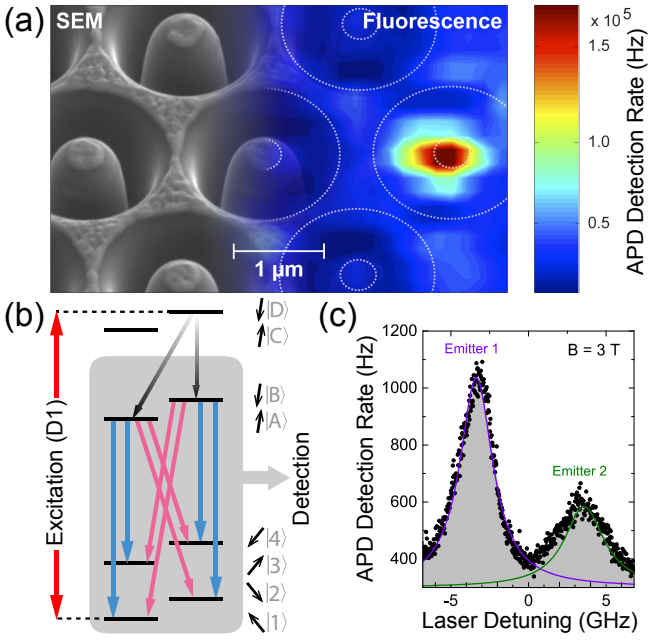

FIG. 2: (Color online) (a) Scanning electron microscope image of the solid immersion lens array on the HPHT sample, superimposed by a corresponding fluorescence image (exc. 690 nm, det. 730-750 nm). (b) Optical excitation is performed resonantly to the highest energy exited state (transition D1, thick red arrow), from where a relaxation to lower excited states (black arrows) occurs, followed by an optical decay to the ground state (red/blue arrows). The emitted fluorescence photons are detected as a function of the excitation frequency. (c) At B = 3 T, resonant excitation reveals the presence of two SiV$^-$ emitters, spectrally separated by approximately 8 GHz.

Single-laser resonant excitation of the D1 transition under 3 T magnetic field resolves the resonances of the two centers spectrally owing to their slightly differing (2%) strain, as shown in Fig. 2(c). This slight variation in the strain tensor between the two centers is used to address each SiV$^-$ selectively. The following experiments are performed using emitter 1 in Fig. 2(c).

If the two transitions of a Λ system are driven simultaneously, the spin is optically pumped into a coherent superposition of the two ground states (dark state) determined by the two optical fields; a technique known as CPT [30]. As a consequence of destructive quantum interference, optical excitation to the shared excited state and, consequently any fluorescence originating from this state, is suppressed. The reduction of the integrated fluorescence, i.e. the CPT dip, is strongly dependent on the coherence between the two ground states and its spectral width allows direct measurement of the coherence timescale of the ground state [30]. Figure 3(a) presents a two dimensional CPT scan for the SiV$^-$ at 0.7 T magnetic field as a function of the optical frequencies of the two lasers driving the D1 and D2 transitions selectively, as illustrated in Fig. 3(b). The two ground states addressed originate from the same orbital branch and have orthogonal spin projections [27]. The manifestation of CPT is evident as a significant drop of the fluorescence intensity at two-photon resonance ($\delta_{L1} - \delta_{L2} = \Delta$, where δ_{L1} and δ_{L2} denote the laser detunings from the D1 and D2 transitions and Δ is the frequency difference between the two states). Figure 3(c) presents the CPT dip obtained by scanning the frequency of the laser driving the D2

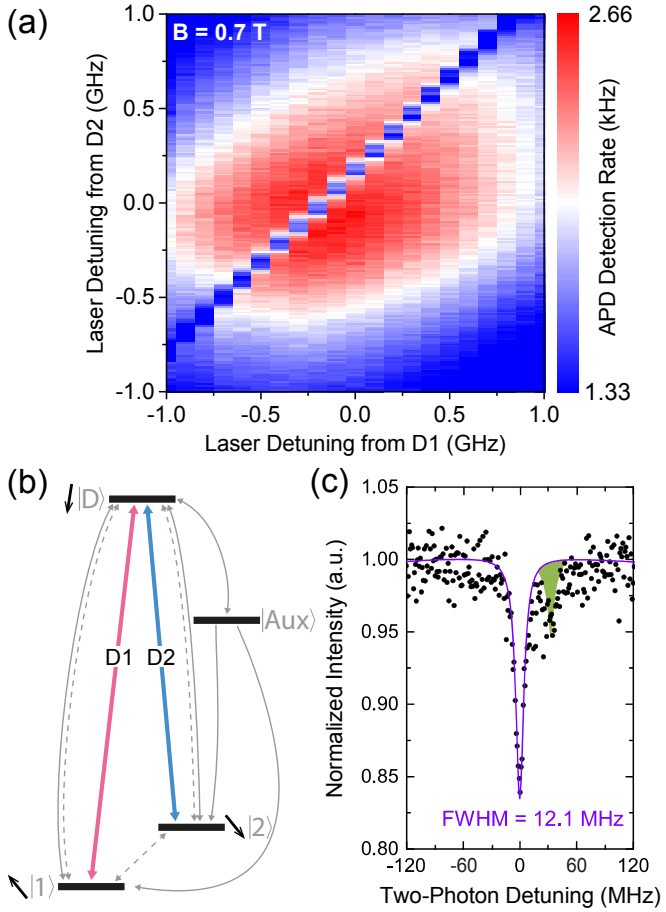

FIG. 3: (Color online) (a) CPT scan: SiV$^-$ fluorescence intensity recorded as the frequency of the laser resonant with transition D2 is scanned and the laser resonant with transition D1 is fixed at a given frequency. Laser powers are equal to approximately four times and seven times the saturation powers for transitions D2 and D1 respectively. (b) Level structure for the simulation of the CPT experiment; transitions D1 and D2 are driven by optical fields (thick, colored arrows). Relaxation and pure dephasing mechanisms are indicated by solid and dashed gray arrows respectively. We add an auxiliary energy level (Aux) to include decays into other channels. (c) CPT scan at low driving power (0.33 µW each, corresponding to the saturation power for the D1 transition and half the saturation power for D2) yielding a dip full width at half maximum of 12.1 MHz. The purple line corresponds to a fit using a model based on optical Bloch equations [27] and giving a decoherence rate between the two ground states of 3.5 ± 0.2 MHz. The green filled curve at slightly higher frequency is the CPT dip of the second SiV$^-$ center.

transition, while keeping the D1 excitation fixed on resonance. In order to extract the ground state coherence time both lasers are kept at sufficiently low excitation powers (equal to saturation power for the D1 transition and half the saturation power for D2) in order to minimize power broadening effects in the CPT dip. Using a Lorentzian fit, the full width at half maximum of the CPT dip under these conditions is 12.1 MHz. This width includes three main contributions: the decoherence in the ground state, the finite mutual coherence of the two lasers and the power broadening described by the Rabi frequencies for the two driven transitions. A theoretical model based on optical Bloch equations [27] which include residual power broadening, spontaneous decays [described by a term $\mathcal{L}(\rho)$] [indicated by solid gray arrows in Fig. 3(b)], pure dephasing [$\mathcal{D}(\rho)$] [dashed gray arrows in Fig. 3(b)] and the coherence of the lasers [$\mathcal{W}(\rho)$], is used to fit the data with the decoherence rate between the two ground states as a free parameter. An auxiliary state allows to describe processes involving states outside the Λ scheme [Fig. 3(b)]. To obtain the populations of the states we numerically solve the master equation

$$\dot{\rho} = -\frac{i}{\hbar}\left[\mathcal{H}_{int}, \rho\right] + \mathcal{L}(\rho) + \mathcal{D}(\rho) + \mathcal{W}(\rho). \qquad (1)$$

We then compare the calculated population in the excited state, which is proportional to the fluorescence, to the experimental data. This analysis provides an upper bound of 3.5 ± 0.2 MHz for the ground states coherence contribution to the dip width and therefore a measure of the SiV$^-$ ground-state coherence time exceeding 45 ns.

The observed coherence time is more than an order of magnitude longer than the timescale for thermalization, which typically takes place within a nanosecond [22]. Hence, we suggest that it is the spin that dictates the decoherence mechanism for the ground states, as the phonon-induced thermalization for ground states of opposite spin is quenched. To support this argument, we take advantage of the presence of an avoided crossing at 3.5 T between two of the ground states. By sweeping the magnetic field over the region of the avoided crossing, we relax the spin state orthogonality, thus progressively allowing for phonon-mediated decoherence of the dark state. Figure 4(a) depicts the evolution of the spin for the ground states coupled by CPT, as the magnetic field is varied over the avoided crossing. From 0 to 3.5 T, the dark state is generated between states $|1\rangle$ and $|2\rangle$, while above 3.5 T the dark state is generated between $|1\rangle$ and $|3\rangle$, as illustrated by the red and blue ribbons respectively [27].

Figure 4(b) shows the linewidth of the CPT dip as a function of the magnetic field ($|1\rangle$ - $|2\rangle$ as red filled circles, $|1\rangle$ - $|3\rangle$ as blue filled circles). This width is proportional to the decoherence rate between the two driven states, on top of a constant power broadening due to the lasers [31]. The dip width increases rapidly when approaching the avoided crossing, and reaches minimum values for both low and high field limits. We calculate the spin-overlap between the two driven states and display it as dashed gray lines Fig. 4(b) [27, 32]. This simple approach already describes the observed trend, emphasizing the central role of the spin orthogonality of the two ground states for decoherence. The spin overlap is multiplied by a Boltzmann factor (red and blue solid lines [27, 32]), thus taking into account the thermal activation of phonons between the addressed ground states, as their energy difference increases with increasing magnetic field. A detailed description of the phonon-mediated mechanism, such as phonon scattering or dynamic Jahn-Teller distortion, can be identified after a temperature-dependent investigation is performed. The agreement between our simple model and the experimental data confirms the hypothesis that the ground state coherence time of 45 ns measured away from the avoided crossing corresponds to the coherence of the spin in the driven ground states. This spin coherence time is identified as the free induction decay time (T_2^*). It is worth noting that the sample employed for the CPT measurement shows evidence for a considerable concentration of substitutional nitrogen [N_S^0] [27], which is known to be the main limitation for T_2^* of the nitrogen vacancy spin [33]. The same mechanism is likely to affect the measured T_2^* for the SiV$^-$ center in addition to phonon-assisted processes. Consequently, this coherence time can be extended using all-optical pulsed protocols analogous to the dynamical decoupling techniques commonly applied to the NV center [34].

In this work, we verified the presence of a spin in the ground state of the SiV$^-$ center in diamond, and probed its coherence using CPT. In order to prepare an arbitrary coherent superposition of the SiV$^-$ spin states, it is possible to implement phase and amplitude modulations of the CPT lasers [25]. Adiabatic manipulation of the superposition can then be achieved using picosecond laser pulses. This also allows for the implementation of all-optical dynamical decoupling schemes, enabling to further extend the coherence time of the spin state. The combination of ultrafast coherent control of individual spins and the high quality and reproducibility of the optical spectrum across multiple SiV$^-$ centers can serve to realize the basic components of a distributed quantum network.

We gratefully acknowledge financial support by the University of Cambridge, the European Research Council (FP7/2007-2013)/ERC Grant agreement no. 209636, FP7 Marie Curie Initial Training Network S^{3}NANO. This research has been partially funded by the European Community's Seventh Framework Programme (FP7/2007-2013) under Grant Agreement N°611143 (DIADEMS). AIT and TG thank EPSRC Programme Grant EP/J007544/1 for support. Ion implantation was performed at and supported by RUBION, central unit of the Ruhr-Universität Bochum. We thank D. Rogalla for the implantation, C. Pauly for SIL fabrication, the

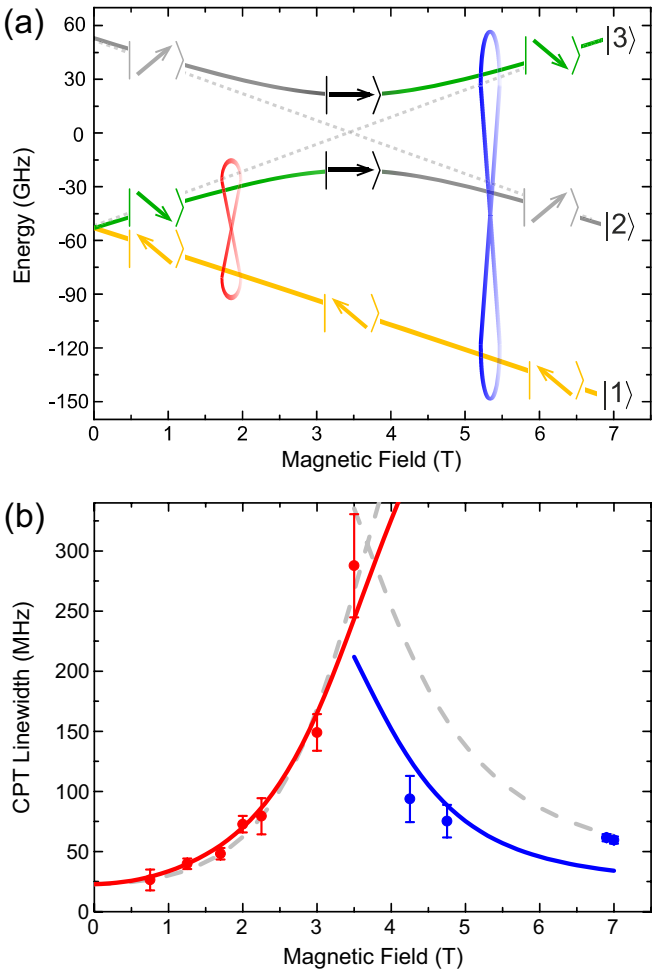

FIG. 4: (Color online) (a) Simulated ground states [27], illustrating the spin state for magnetic field values below, above and at the avoided crossing (3.5 T). (b) Full width at half maximum of the CPT dip as a function of the magnetic field, using a Lorentzian fit. Filled circles denote measured widths (for each transition, laser powers equal to four times the saturation power), with the error bars being the standard deviation of multiple measurements. The solid lines display the spin overlap (grey dashed lines) between states used for CPT, multiplied by a Boltzmann factor [27]. In panels (a) and (b), the color red (blue) indicates CPT realized between states $|1\rangle$ and $|2\rangle$ for $B < 3.5\,\mathrm{T}$ (between $|1\rangle$ and $|3\rangle$ for $B > 3.5\,\mathrm{T}$).

Sheffield group for their hospitality during the vector magnet measurements, A. Lenhard for the Monte-Carlo simulation of the intensity autocorrelation, as well as J. Barnes, J. Hansom, H. S. Knowles, J. M. Taylor, J. Eschner and G. Morigi for helpful discussions.

Note: During the revision of this manuscript, we became aware of complementary work reporting similar findings [35].

* These authors contributed equally to this work.

† Electronic address: christoph.becher@physik.uni-saarland.de, ma424@cam.ac.uk

[1] A. M. Zaitsev, Optical Properties of Diamond: A Data Handbook (Springer-Verlag, Berlin, 2001).
[2] P. Prawer and I. Aharonovich, Quantum information processing with diamond: Principles and applications (Woodhead Publishing, 2014).
[3] C. D. Clark and C. A. Norris, J. Phys. C Solid State Phys. **4**, 2223 (1971).
[4] V. Acosta and P. Hemmer, MRS Bulletin **38**, 127 (2013).
[5] M. W. Doherty, N. B. Manson, P. Delaney, F. Jelezko, J. Wrachtrup, and L. C. Hollenberg, Phys. Rep. **528**, 1 (2013).
[6] L. Childress and R. Hanson, MRS Bull. **38**, 134 (2013).
[7] I. Aharonovich and E. Neu, Advanced Optical Materials, DOI: 10.1002/adom.201400189 (2014).
[8] J. R. Maze, A. Gali, E. Togan, Y. Chu, A. Trifonov, E. Kaxiras, and M. D. Lukin, New J. Phys. **13**, 025025 (2011).
[9] M. Doherty and N. Manson, New J. Phys. **13**, 025019 (2011).
[10] A. Gruber, A. Dräbenstedt, C. Tietz, L. Fleury, J. Wrachtrup, and C. v. Borczyskowski, Science **276**, 2012 (1997).
[11] F. Dolde, V. Bergholm, Y. Wang, I. Jakobi, B. Naydenov, S. Pezzagna, J. Meijer, F. Jelezko, P. Neumann, T. Schulte-Herbrüggen, J. Biamonte, and J. Wrachtrup, Nat. Commun. **13**, 3371 (2014).
[12] L. Li, T. Schröder, E. H. Chen, M. Walsh, I. Bayn, J. Goldstein, O. Gaathon, M. E. Trusheim, M. Lu, J. Mower, M. Cotlet, M. Markham, D. J. Twitchen, and D. Englund, arxiv:1409.1602.
[13] I. Aharonovich, A. D. Greentree, and S. Prawer, Nat. Photonics **5**, 397 (2011).
[14] A. Faraon, C. Santori, Z. H. Huang, V. M. Acosta, and R. G. Beausoleil, Phys. Rev. Lett. **109**, 033604 (2012).
[15] B. Hausmann, B. Shields, Q. Quan, Y. Chu, N. de Leon, R. Evans, M. Burek, A. Zibrov, M. Markham, D. Twitchen, H. Park, M. Lukin, and M. Loncar, Nano Letters **13**, 5791 (2013).
[16] E. Neu, D. Steinmetz, J. Riedrich-Möller, S. Gsell, M. Fischer, M. Schreck, and C. Becher, New J. Phys. **13**, 025012 (2011).
[17] J. Riedrich-Möller, C. Arend, C. Pauly, F. Mücklich, M. Fischer, S. Gsell, M. Schreck, and C. Becher, Nano Letters, DOI: 10.1021/nl502327b (2014).
[18] A. Sipahigil, K. D. Jahnke, L. J. Rogers, T. Teraji, J. Isoya, A. S. Zibrov, F. Jelezko, and M. D. Lukin, Phys. Rev. Lett. **113**, 113602 (2014).
[19] L. Rogers, K. Jahnke, T. Teraji, L. Marseglia, C. Müller, B. Naydenov, H. Schauffert, C. Kranz, J. Isoya, L. McGuinness, and F. Jelezko, Nat. Commun. **5**, 4739 (2014).
[20] W. Pfaff, B. Hensen, H. Bernien, S. van Dam, M. Blok, T. Taminiau, M. Tiggelman, R. Schouten, M. Markham, D. Twitchen, and R. Hanson, Science **345**, 532 (2014).
[21] A. Sipahigil, M. Goldman, E. Togan, Y. Chu, M. Markham, D. Twitchen, A. Zibrov, A. Kubanek, and

M. Lukin, Phys. Rev. Lett. **108**, 143601 (2012).
[22] T. Müller, C. Hepp, B. Pingault, E. Neu, S. Gsell, M. Schreck, H. Sternschulte, D. Steinmüller-Nethl, C. Becher, and M. Atatüre, Nat. Commun. **5**, 3328 (2014).
[23] C. Santori, P. Tamarat, P. Neumann, J. Wrachtrup, D. Fattal, R. Beausoleil, J. Rabeau, P. Olivero, A. Greentree, S. Prawer, F. Jelezko, and P. Hemmer, Phys. Rev. Lett. **97**, 247401 (2006).
[24] C. G. Yale, B. B. Buckley, D. J. Christle, G. Burkard, F. J. Heremans, L. C. Bassett, and D. D. Awschalom, Proc. Natl. Acad. Sci. U. S. A. **110**, 7595 (2013).
[25] J. Hansom, C. Schulte, C. Le Gall, C. Matthiesen, E. Clarke, M. Hugues, J. Taylor, and M. Atatüre, Nat. Physics **10**, 725 (2014).
[26] H. Sternschulte, K. Thonke, R. Sauer, P. C. Münzinger, and P. Michler, Phys. Rev. B **50**, 14554 (1994).
[27] See Supplemental Material at [URL will be inserted by publisher] for details on experimental setup, sample characterization and spin state representation.
[28] J. P. Goss, R. Jones, S. Breuer, P. Briddon, and S. Öberg, Phys. Rev. Lett. **77**, 3041 (1996).
[29] C. Hepp, T. Müller, V. Waselowski, J. N. Becker, B. Pingault, H. Sternschulte, D. Steinmüller-Nethl, A. Gali, J. R. Maze, M. Atatüre, and C. Becher, Phys. Rev. Lett. **112**, 036405 (2014).
[30] M. Fleischhauer, A. Imamoglu, and J. P. Marangos, Rev. Mod. Phys. **77**, 633 (2005).
[31] S. Gateva, E. Alipieva, and E. Taskova, Phys. Rev. A **72**, 025805 (2005).
[32] A scaling factor and an offset, common to both sides of the curve, are used for display along with the CPT width.
[33] F. Jelezko, T. Gaebel, I. Popa, A. Gruber, and J. Wrachtrup, Phys. Rev. Lett. **92**, 076401 (2004).
[34] G. de Lange, Z. H. Wang, D. Ristè, V. V. Dobrovitski, and R. Hanson, Science **330**, 60 (2010).
[35] L. Rogers, K. Jahnke, M. Metsch, A. Sipahigil, J. Binder, T. Teraji, H. Sumiya, J. Isoya, M. Lukin, P. Hemmer, and F. Jelezko arxiv:1410.1355.

Supplemental Material: All-optical formation of coherent dark states of silicon-vacancy spins in diamond

Benjamin Pingault,[1,*] Jonas N. Becker,[2,*] Carsten H. H. Schulte,[1] Carsten Arend,[2] Christian Hepp,[1] Tillman Godde,[3] Alexander Tartakovskii,[3] Matthew Markham,[4] Christoph Becher,[2,†] and Mete Atatüre[1,†]

[1] *Cavendish Laboratory, University of Cambridge, JJ Thomson Ave, Cambridge CB3 0HE, UK*
[2] *Fachrichtung 7.2 (Experimentalphysik), Universität des Saarlandes, Campus E2.6, 66123 Saarbrücken, Germany*
[3] *Department of Physics and Astronomy, University of Sheffield, Sheffield S3 7RH, UK*
[4] *Element Six Ltd., Global Innovation center, Fermi Avenue, Harwell Oxford, Didcot, OX11 0QR, UK*

(Dated: October 29, 2014)

I. SAMPLE PREPARATION AND EXPERIMENTAL SETUPS

A. Sample preparation

In this work, two different samples were investigated. The first ["(001) sample"] is a high-purity ($[N]_s^0 < 5\,\mathrm{ppb}$, $[B] < 1\,\mathrm{ppb}$) diamond produced by chemical vapor deposition (electronic grade from Element Six) with a (001) surface orientation. The second sample ["(111) sample"] is a type IIa HPHT diamond (Element Six) with a (111) main surface. In both samples, SiV^- centers were created by ion implantation of $^{28}Si^+$ ions at an energy of 900 keV and doses between 10^9 and 10^{12} ions $\cdot\,\mathrm{cm}^{-2}$. Simulations using the stopping range of ions in matter algorithm [1] showed that the Si^+ stop at 500 ± 50 nm below the diamond surface. Following the implantation, the samples were annealed at 1000°C in vacuum for 3 hours, followed by an oxidation step in air for 1 hour at 460°C. The creation efficiency for SiV^- centers was found to be different in the two samples: Single SiV^- centers have been found in the 10^{10} ions $\cdot\,\mathrm{cm}^{-2}$ region for the (001) sample and in the 10^9 ions $\cdot\,\mathrm{cm}^{-2}$ region for the (111) sample.
Due to refraction and total internal reflection at the diamond-air interface, the collection efficiency of defect centers in bulk diamond samples is considerably lower compared to previously reported measurements on nanodiamonds [2]. To enhance the collection efficiency, arrays of solid immersion lenses (SILs, cf. Fig. S1 (a) and Fig. 2 (a) of the main text) were milled into the samples surfaces using a focused ion beam (FIB). A cross section measurement of an individual SIL (Fig. S1 (b)) shows a mean diameter of 500 nm, hence the focal point of the SIL matches the implantation depth of the SiV^- centers. After the milling, a post-treatment according to reference [3] was applied to remove graphite residues and gallium incorporated into the diamond surface during the FIB process. Measurements on former samples showed an increase of collection efficiency by a factor 3 to 5 [4].

In a preliminary experiment, the (111) sample showed fluorescence from NV^- centers upon excitation at 532 nm. The emission is observed homogeneously over the sample, and is increased in the region of the SIL arrays. This is a strong indication, that the sample contains nitrogen, most likely in substitutional form (referred to as $[N_S^0]$ or P1 [5]). A fraction of the substitutional nitrogen is transformed into NV^- centers during the HPHT growth. In addition, the FIB milling is known to create additional vacancies. During the annealing step, which we perform after FIB milling, the mobility of these lattice vacancies is sufficiently increased and a migration towards nitrogen impurities leads to the formation of NV defect complexes. This explains the higher abundance of NV^- centers in the vicinity of the FIB treated areas. The paramagnetic substitutional nitrogen in diamond is known to be one of the main sources of decoherence for the spin of the NV^- center and limits its T_2^* time [6].

B. Experimental setups

For the spectroscopic investigation and the coherent population trapping, two experimental setups have been employed. The first setup was utilized to measure the SiV^- fine structure spectrum as a function of the orientation and magnitude of an applied magnetic field (cf. Fig 1 of the main text). It consists of a confocal microscope mounted on a helium bath cryostat equipped with a vector magnet. The sample was mounted on a stack of piezoelectric stages allowing translations in three spacial directions. The cryostat was operated at a temperature of 4 K. The (001)-sample

* These authors contributed equally to this work.

† Electronic address: christoph.becher@physik.uni-saarland.de, ma424@cam.ac.uk

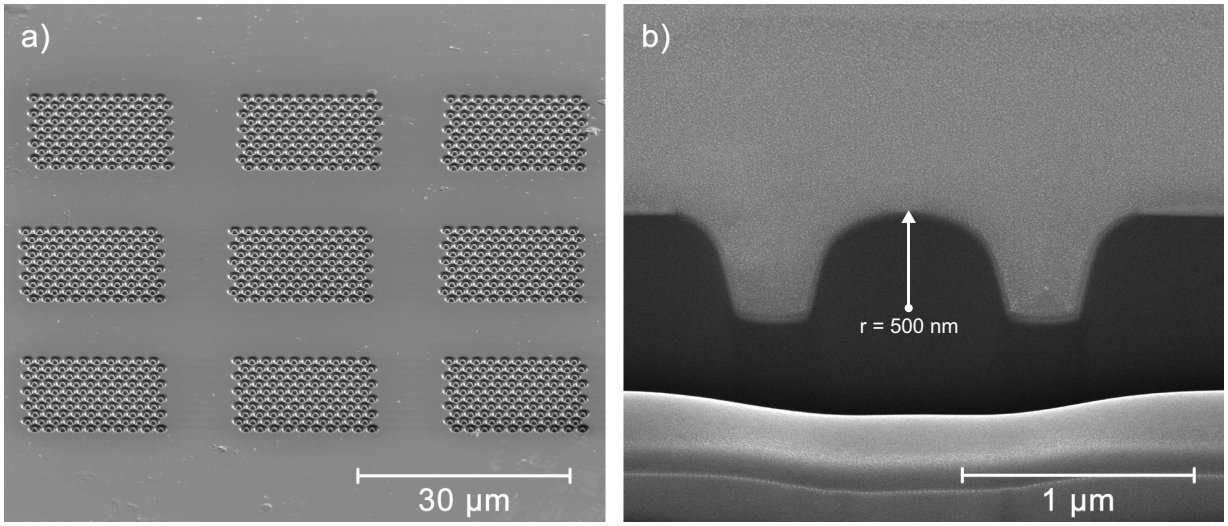

FIG. S1. (a,b) SEM images of the fabricated solid immersion lenses (SILs). Nine fields of 10×10 SILs have been created using focussed ion beam (FIB) milling (a). The radius of the (hemispheric) SILs matches the implantation depth of the SiV^- centers, each SIL is surrounded by a 300 nm wide trench to avoid light scattering at the edges of the FIB cut (b).

was placed at the center of superconducting coils allowing to apply a magnetic field of up to 9 T along the vertical axis of the cryostat (corresponding to the [001] crystal direction investigated in the (001) diamond sample) and up to 4.5 T along any other axis within a vertical plane. A single SiV^- center was excited non-resonantly at 690 nm using a diode laser. The laser was focused onto the sample through a single aspheric lens (NA = 0.68, f = 3.1 mm). The fluorescence was collected through the same lens and sent to a double slit spectrometer with a resolution of 0.009 nm. This experimental setup was used to investigate the (001) sample.

The coherent population trapping experiments were performed using a similar confocal microscope. The (111)-sample was cooled to liquid helium temperature in a bath cryostat. A magnetic field up to 7 T could be applied along the vertical axis of the cryostat (corresponding to the [111] crystal axis which forms an angle of 109.4° with the SiV^- center studied) using a superconducting coil. The resonant driving of two optical transitions was performed using two tunable diode lasers focused onto the sample with a single aspheric lens (NA = 0.68, f=3.1 mm). The fluorescence was collected through the same lens and sent to a filtering setup where the reflected laser light was separated from the fluorescence using a grating (1600 grooves/mm). The fluorescence was then sent to an avalanche photodiode. This experimental setup was used to investigate the (111) sample. The two excitation lasers were stabilized to a wavemeter (Highfinesse WS-U), and show a mutual coherence of about 5 MHz in linear frequency for integration times between 0.5 s and 8 s typically used during our CPT measurements.

II. SIV^- CHARACTERIZATION

In this section, we provide a comprehensive characterization of the individual SiV^- centers studied in the main paper. First, we compare the fluorescence spectrum as a function of magnetic field (referred to as "Zeeman spectrum") depicted in Fig. 1 of the main text to a group theoretical simulation (Sec. II A). These spectra have been obtained by applying magnetic fields to an individual SiV^- center in the (001) sample. From the comparison with the simulation, we obtain the eigenstates of the center for the different magnetic field configurations. Second, we investigate the emitter used for CPT [in the (111) sample] by analyzing its Zeeman spectrum, its fluorescence lifetime and its intensity autocorrelation (Sec. II B).

A. Modeling of the magnetic field orientation dependence of the optical transitions

The Zeeman spectra of the emitter in the (001) sample depicted in Fig. 1 of the paper are compared to the theoretical model of the SiV^- center described in [4]. The model calculates the energy levels of the SiV^- center, taking into account spin-orbit, Jahn-Teller, strain and Zeeman interactions. Optical transitions between the resulting states are calculated and compared to the Zeeman spectra. The presentation of the experimental Zeeman spectra in Figs. S2

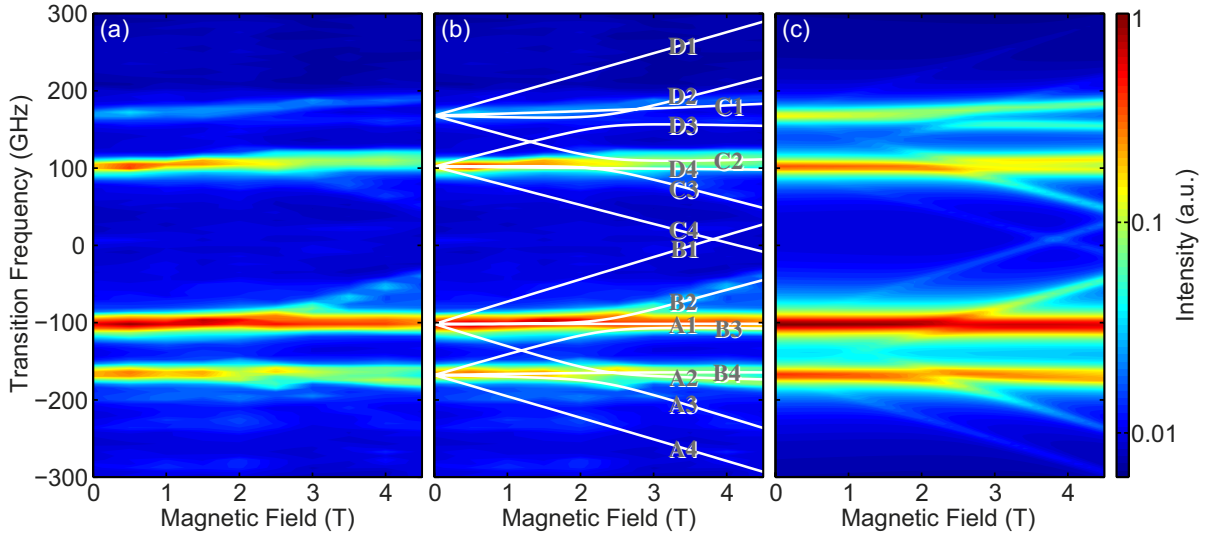

FIG. S2. Zeeman spectrum for a magnetic field along the [111] crystal direction. (a) Experimental spectra alone, (b) overlapped with simulated transition wavelengths (white lines). (c) Fully simulated spectra as a function of magnetic field. An angle of 10° between magnetic field and SiV$^-$ axes fits best the experimental data. The labels for the optical transitions in panel (b) correspond to the black arrows connecting the SiV$^-$ energy levels displayed in Fig. S5(a).

- S4 and S8 follows the conventions of Ref. [4], i.e., the left panel shows the experimental Zeeman spectrum alone, the middle panel shows the experimental spectrum together with the simulated transitions (as white solid lines) and the right panel shows a simulated Zeeman spectrum. In the latter, the optical transitions, considered as dipolar electric and predicted by the theoretical model, have relative peak intensities which are proportional to the optical dipole matrix elements and thermal population of the energy levels involved. The dipole matrix elements in turn depend on the orbital and spin parts of the wave function, where transitions between opposite spin (S_z) projections are forbidden.

a. [111] *orientation of the magnetic field:* Figure 1(b) of the paper shows the case of a magnetic field aligned approximately along the [111] crystal axis, which is the high symmetry axis of the SiV$^-$ center investigated. The Zeeman spectrum is displayed in Fig. S2 for the following analysis. In Fig. S2(a) we observe that the transitions of the SiV$^-$ fine structure spectrum only respond weakly to the increasing magnetic field. Panel S2(b) reveals that there are more possible optical transitions, i.e. each peak can in principle split into four components. However, out of these four components only a fraction is visible. To elucidate why several optical transitions are not observed, we refer to the SiV$^-$ level splitting in the [111] magnetic field configuration depicted in Fig. S5(a). We can write the SiV$^-$ electronic states as superpositions of spin-up and spin-down basis states, i.e. $|k\rangle = c_{\uparrow}^{(k)}|\uparrow\rangle + c_{\downarrow}^{(k)}|\downarrow\rangle$, where $k = 1, \ldots, 4$ for the ground state and $k = A, \ldots, D$ for the excited state. In this representation, we neglect the orbital part of the wave function, and we illustrate the resulting spin superposition state as a Bloch vector (for a detailed discussion of the Bloch sphere representation, see Sec. IV). As a simplified illustration, we depict the deviation of the Bloch vector from the poles of the sphere as a tilted arrow in the figures of the main paper as well as in Figs. S5.

In general, the coefficients $c_{\uparrow,\downarrow}^{(k)}$ depend on the magnetic field strength. For small magnetic fields ($B < 2$ T), the simulation shows that the ground states $|1\rangle$ and $|2\rangle$, as well as $|3\rangle$ and $|4\rangle$ have pairwise opposite spins, i.e. $\left|c_{\uparrow}^{(1,3)}\right|^2 \approx 0$, $\left|c_{\downarrow}^{(1,3)}\right|^2 \approx 1$ for states $|1\rangle$, $|3\rangle$, and vice versa for states $|2\rangle, |4\rangle$. A similar situation is present for the excited state. As a consequence, the dipole transitions between states of opposite spin projections are forbidden and these peaks are observed neither in the experimental nor in the simulated spectra [Fig. S2(c)]. An example is the forbidden transition from excited state $|A\rangle$ to ground state $|4\rangle$, which we denote as $A4$.

At $B \approx 2.2$ T, the levels $|2\rangle$ and $|3\rangle$ show an avoided crossing. Here, the spin-up- and spin-down coefficients for state $|2\rangle$ and state $|3\rangle$, respectively, are approximately equal, i.e. $\left|c_{\uparrow}^{(2)}\right|^2 \approx \left|c_{\downarrow}^{(2)}\right|^2$ and $\left|c_{\uparrow}^{(3)}\right|^2 \approx \left|c_{\downarrow}^{(3)}\right|^2$. Hence, the expectation values $\langle S_z\rangle$ of the S_z spin components of the two states are equal to zero, and optical transitions become allowed for this magnetic field value. For higher magnetic fields $B > 3$ T, the S_z projections for states $|2\rangle$ and $|3\rangle$ are swapped. In consequence, several transitions, e.g. $A2$, are now allowed and are observed in the spectrum.

It is important to note that the avoided crossing observed in the Zeeman spectrum is not a consequence of the

spin-orbit coupling; in fact, the spin-orbit Hamiltonian derived in Ref. [4] has no interaction terms between states of opposite spin. Instead, the transverse spin coupling terms S_x, S_y are present in the Zeeman Hamiltonian, i.e. $\mathcal{H}^{\mathrm{Z,S}} \propto (S_x B_x + S_y B_y + S_z B_z)$, where the subscripts x, y, z refer to the internal coordinate system of the SiV$^-$ center [4]. For a magnetic field, which is perfectly aligned with the high symmetry axis of the SiV$^-$ center, all states have unity spin polarization and no avoided crossing is expected. Due to a 10° misalignment of the magnetic field with respect to the SiV$^-$ axis in the experiment presented here, we observe the aforementioned avoided crossing in Fig. S5(a). As a further consequence of this slight misalignment all electronic states are superpositions of spin-up and spin-down components, although for each state, one spin component is largely dominant. This leads to the observation of transitions $A3$, $B2$, $C3$, $D2$ at high magnetic fields [Fig. S2], which would not be observed for a perfectly aligned magnetic field.

The SiV$^-$ center, which we refer to in Fig. S2, is subject to crystal strain, most likely induced by the SIL carving process. Crystal strain leads to an additional splitting of the spectral fine structure. Hence, by comparing the observed fine structure spectrum at $B = 0$ T to the one observed for low-strain SiV$^-$ centers in Refs. [4, 7], we identify the additional splitting caused by crystal strain. For the emitter in the (001) sample shown in Figs. S2 - S4, the excited state splitting is increased by 20 GHz, and the ground state by 13 GHz. In the framework of the theoretical model presented in [4], crystal strain can be modeled for SiV$^-$ centers as a purely orbital interaction which does not influence the spin part of the wave function.

b. [001] *orientation of the magnetic field:* An orientation of the magnetic field along the [001] crystal axis corresponds to an angle of about 54.7° between the field and the SiV$^-$ high symmetry axis (Fig. S3). The resulting level scheme for this field configuration [Fig. S5(b)] has been discussed in detail in Ref. [4]. It was shown that the excited state exhibits still a high spin polarization, whereas all ground states are superpositions of the spin-up and spin-down components. Hence, most optical transitions are observed and the Zeeman spectrum (Fig. S3) shows a number of 16 transitions.

c. $[\bar{1}\bar{1}1]$ *orientation of the magnetic field:* The spin polarization of both ground and excited states is further reduced, with the magnetic field aligned along the $[\bar{1}\bar{1}1]$ direction (equivalent to an angle of about 109.4° with the SiV$^-$ axis). In comparison to the Zeeman spectrum for [001], we observe for the $[\bar{1}\bar{1}1]$ field orientation (Fig. S4) that the optical transitions are less split, i.e. we observe a smaller effective g-factor for the magnetic field splitting. We stress, that the simulations for the Zeeman spectra of all three field orientations were obtained by only varying the relative angle between the magnetic field and the SiV$^-$ high symmetry axis without adjusting any other parameter of the simulation. The excellent agreement between experiment and simulation proves the accuracy of the SiV$^-$ model which we employ for the current investigations.

In summary, we observe that the presence or absence of optical transitions in the Zeeman spectra depends on the relative angle between the SiV$^-$ high symmetry axis and the magnetic field direction. To underline this point, we simulate the evolution of optical transitions as a function of the magnetic field angle in Fig. S6. The simulation again takes the optical selection rules into account, and is shown for magnetic field strengths of 2 T and 7 T. The most striking feature is the disappearance of several optical transitions as the angle goes to zero. These transitions would occur between states of different spin and are therefore forbidden.

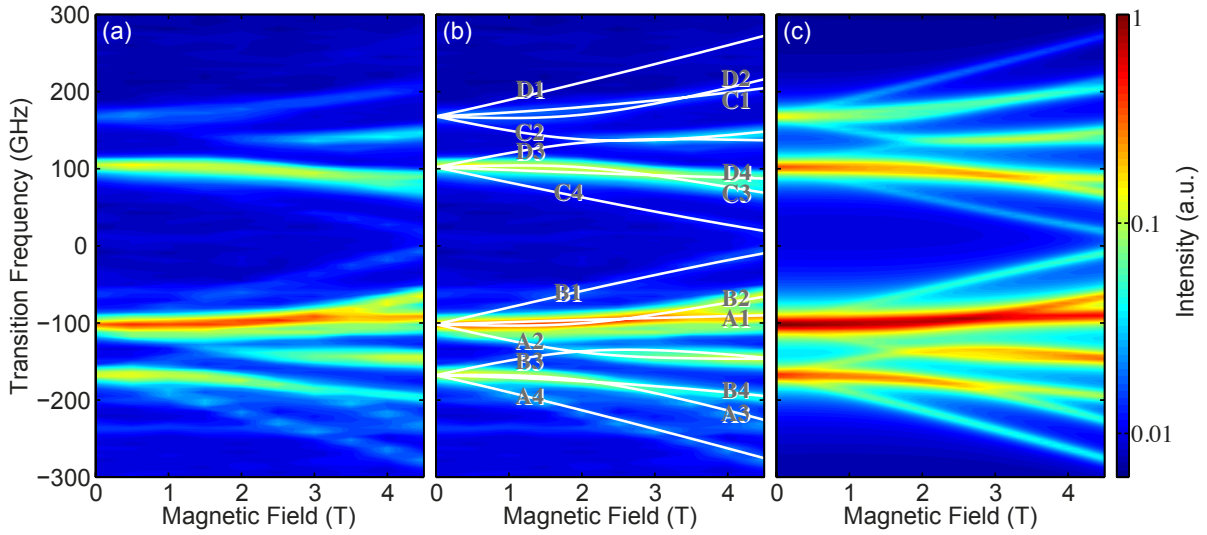

FIG. S3. Zeeman spectrum for a magnetic field along the [001] crystal direction, corresponding to a relative angle of 54.7° between the high symmetry axis of the SiV center and the magnetic field direction. (a) Experimental spectra alone, (b) overlapped with simulated transition wavelengths (white lines). (c) Fully simulated spectra as a function of magnetic field. The labels for the optical transitions in panel (b) correspond to the black arrows connecting the SiV^- energy levels displayed in Fig. S5(b).

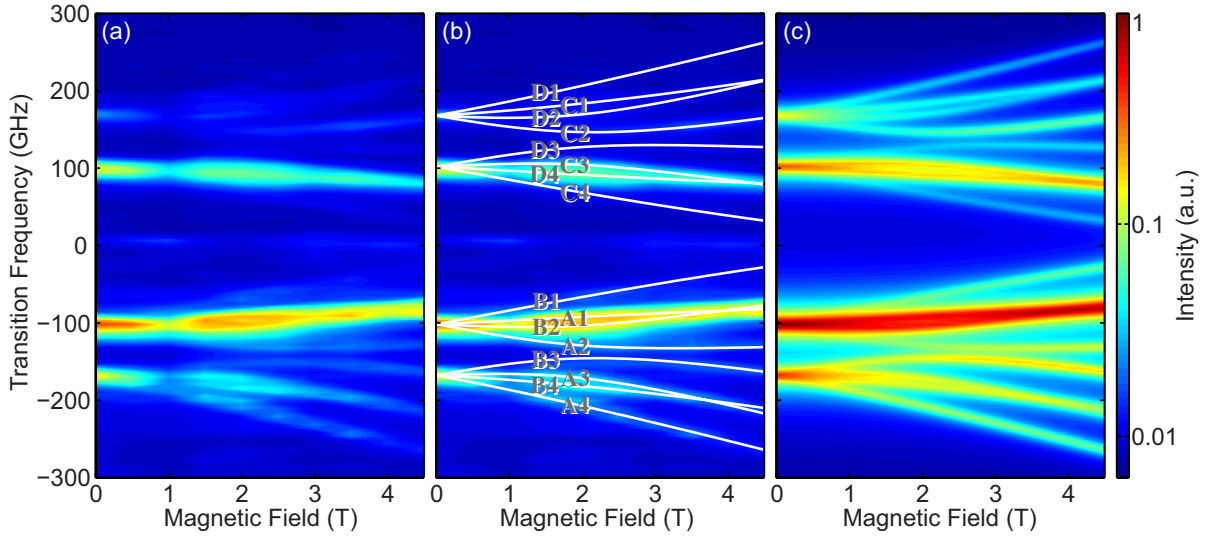

FIG. S4. Zeeman spectrum for a magnetic field along the $[\bar{1}\bar{1}1]$ crystal direction, corresponding to a relative angle of 109.4° between the high symmetry axis of the SiV center and the magnetic field direction. (a) Experimental spectra alone, (b) overlapped with simulated transition wavelengths (white lines). (c) Fully simulated spectra as a function of magnetic field. The labels for the optical transitions in panel (b) correspond to the black arrows connecting the SiV^- energy levels displayed in Fig. S5(c).

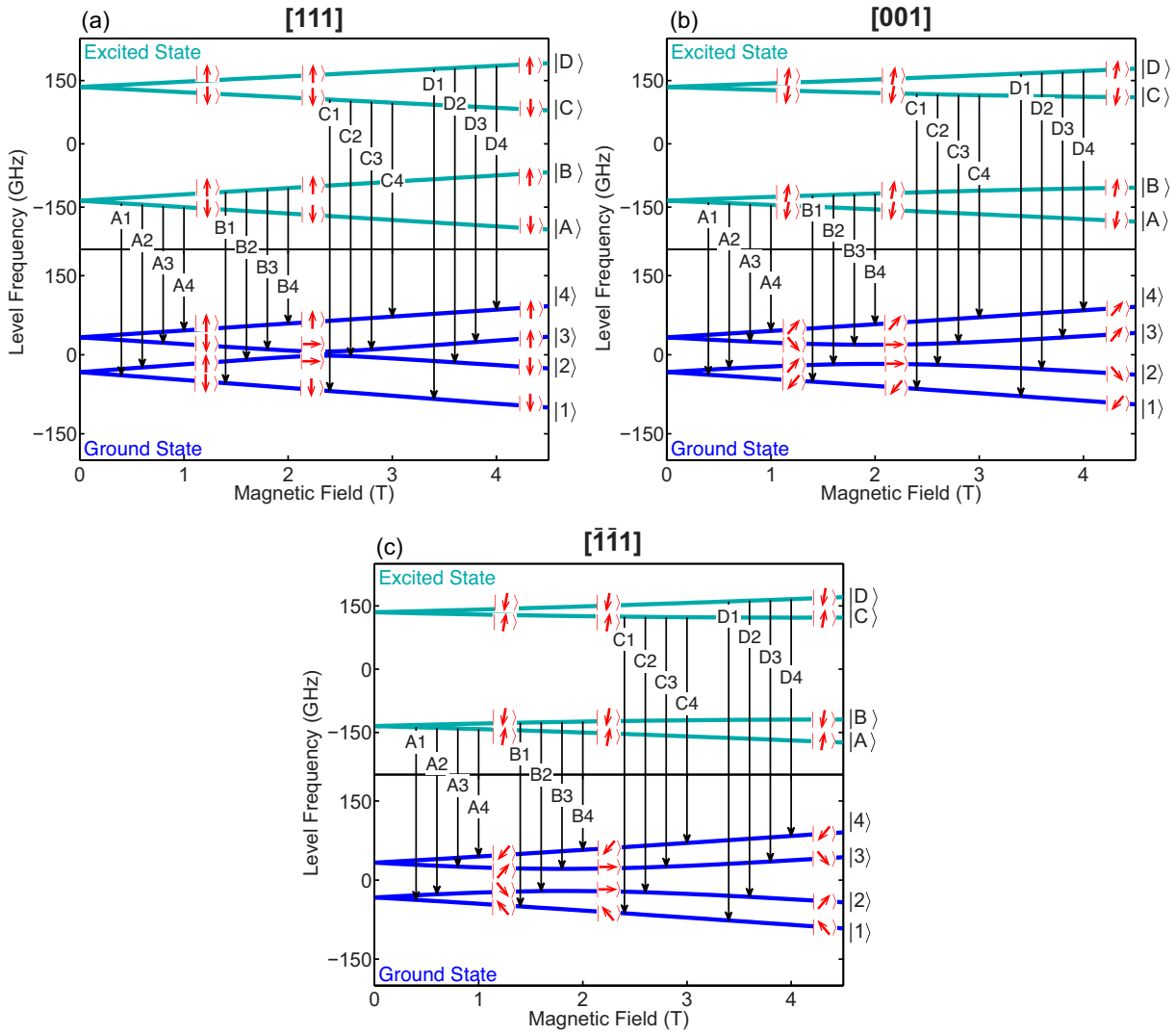

FIG. S5. Calculated level schemes of an SiV^- center in the (001) sample for magnetic fields aligned along the [111] (a), the [001] (b) and the [$\bar{1}\bar{1}$1] crystal direction (c). The red arrows indicate the spin states of the levels, black arrows mark the optical transitions.

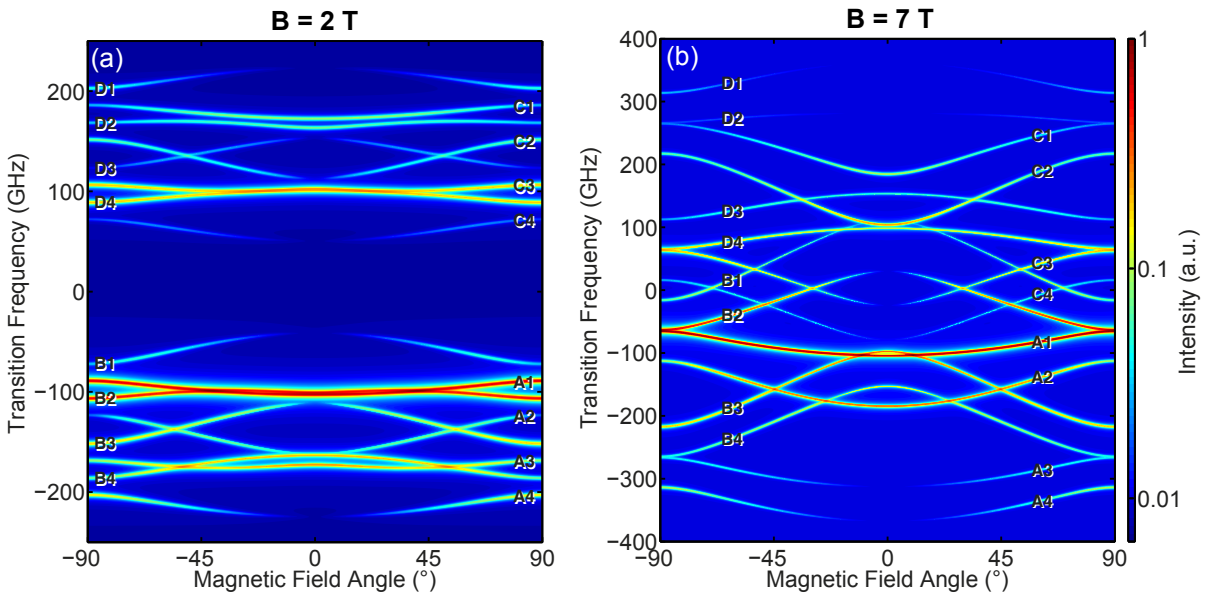

FIG. S6. Simulated spectra of the SiV^- fine structure for the variation of the polar angle between the high symmetry axis of the SiV^- and the magnetic field at (a) 2 T and (b) 7 T. For magnetic fields which are not aligned with the main axis of the emitter, spin forbidden transitions A2, A4, B1, B3, C2, C4, D1, D3 become visible. In D_{3d} symmetry the Zeeman perturbation of the SiV^- energy levels is cylindrically symmetric and therefore only depends on the azimuthal angle of the magnetic field with respect to the high symmetry axis of the emitter.

B. Characterization of the SiV$^-$ center used for CPT

The SiV$^-$ center used for CPT is located below a solid immersion lens in the (111) diamond sample. This center has been chosen because of its comparatively high brightness with up to $3 \cdot 10^5$ counts/s under non-resonant excitation. A measurement of the intensity autocorrelation function $g^{(2)}(\tau)$, shown in Fig. S7 (a) was performed under pulsed non-resonant excitation at 705 nm with a pulse width of 150 fs. The measured data is indicated by black circles and the red solid line shows a Monte Carlo simulation of two emitting defects similar to the approach shown in [8]. In this simulation, only the intensity ratio between both emitters is used as a free parameter. This ratio has been determined to be approximately 2:1, which is in good agreement with the measured PLE spectra. The simulation also takes into account the APD timing jitter of 354 ps. The value of $g^{(2)}(0) = 0.58$ confirms the presence of a second SiV$^-$, evidenced in the photoluminescence excitation measurement shown in Fig. 2 (c) of the main text.

The lifetime of the excited state of the center was determined by a time-correlated single photon counting experiment, as shown in Fig. S7 (b). A fit with a single exponential decay gives a value of 1.66 ns. This lifetime is used to determine the transition rates in the optical Bloch equation model. The absence of a second rate arising from the second emitter is likely due to a similar lifetime.

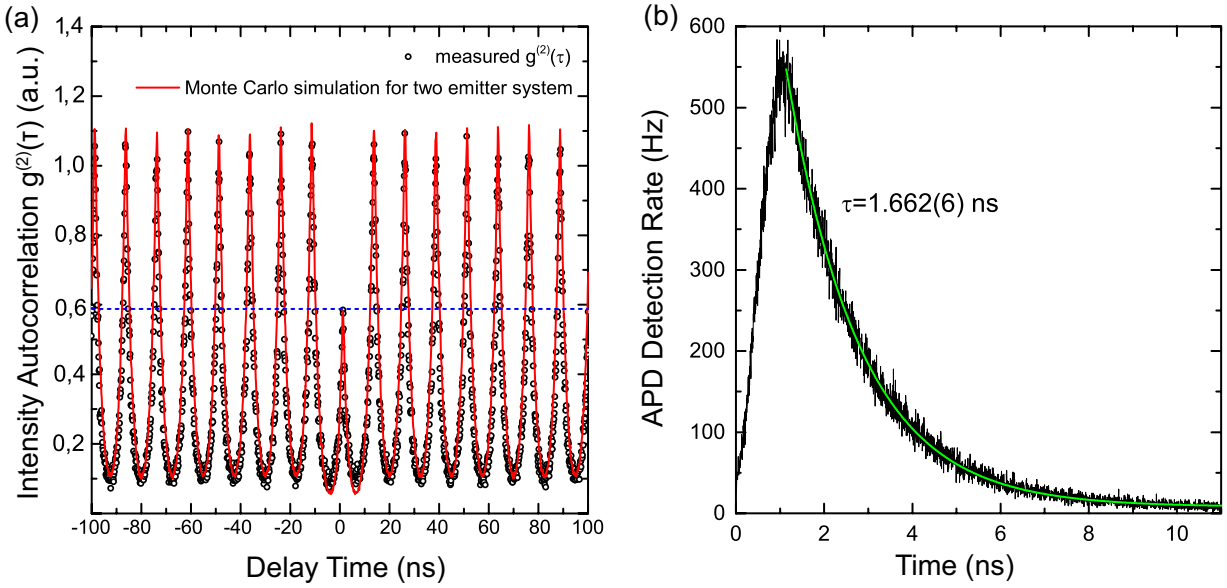

FIG. S7. (a) Pulsed autocorrelation measurement for the emitter used in CPT experiments. The zero delay value of 0.59 is consistent with the presence of a second SiV$^-$ center. (b) Time-correlated single photon counting experimental data on the same SiV$^-$ center. The relaxation is fitted using a single exponential giving a relaxation decay time of (1.662 ± 0.006) ns.

The experimental magnetic field dependence of the SiV$^-$ center used for CPT is displayed in Fig. S8. The emitter is oriented along the $[\bar{1}\bar{1}1]$ direction and forms a relative angle of 109.4° with the magnetic field (applied along the [111] direction). Hence, the angle between the magnetic field and the emitter is similar to the one depicted in Fig. S4. Figure S8(b) shows the simulated optical transitions (as solid white lines) printed on top of the experimental data. As another feature, we notice the presence of anticrossings at about 3.5 T. We observe a few extra transitions, which however have significantly lower intensity. These optical transitions originate from the second center, which was identified in the intensity autocorrelation measurements described above. Similar to the SiV$^-$ center described in Sec. II A, the emitter employed for CPT is subject to crystal strain, which leads to an additional splitting of the fine structure spectrum (36 GHz for the ground state, and 58 GHz for the excited state).

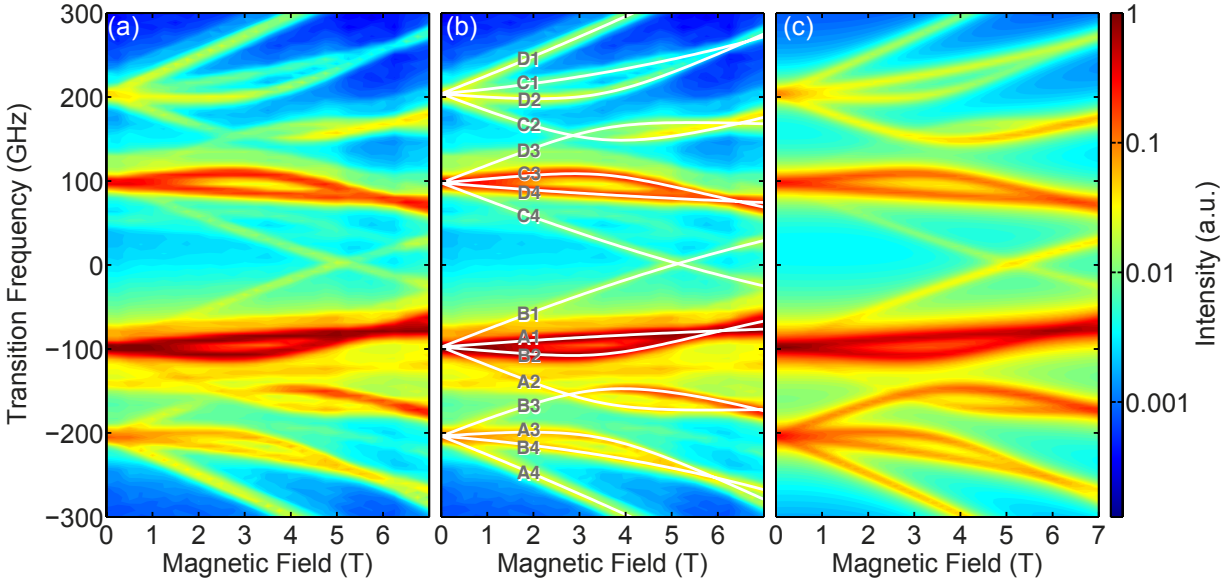

FIG. S8. (a) Experimental fluorescence spectra as a function of the applied magnetic field for the SiV^- center within the (111) sample used in CPT experiments. The magnetic field has a relative angle of 109.4° to the SiV^- axis. (b) Simulated transition wavelengths (white lines) based on [4], superimposed with experimental data. Transition labels correspond to the energy levels displayed in Fig. S9. (c) Fully simulated spectra as a function of magnetic field for an angle of 109.4° between magnetic field and SiV^- axes.

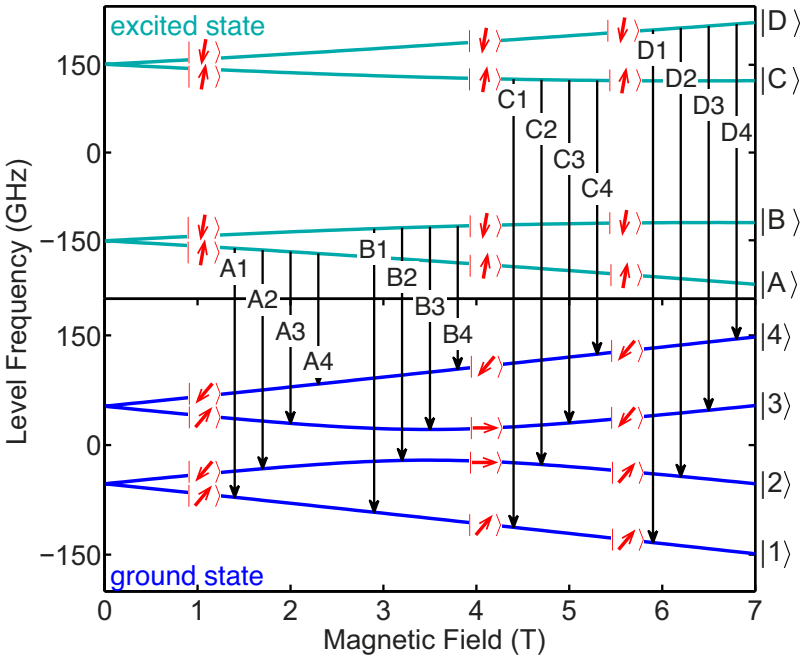

FIG. S9. Calculated level scheme of the SiV^- center in the (111) sample used for CPT experiments for a magnetic field aligned under a relative angle of 109.4° to the high symmetry axis of the emitter. The red arrows indicate the spin states of the levels, black arrows mark the optical transitions.

III. OPTICAL BLOCH EQUATION MODEL

We model the dynamics of the SiV$^-$ center using an open Λ type system including two ground states 1 and 3, the excited state 2 and an auxiliary state 4 (this is the standard labeling of states used in literature and should not be confused with the labeling of the energy levels of the SiV$^-$ center). State 4 is used to model additional decay channels due to relaxations from the excited state of the Λ system to other excited states of the SiV$^-$ (the transitions from these states are used for detection). Population leaking from the Λ system into this auxiliary state doesn't influence the coherence time (i.e. the CPT dip width) of the ground state superposition but reduces the contrast of the observed CPT dip. In the next paragraph, we further specify the transitions driven between the electronic states.

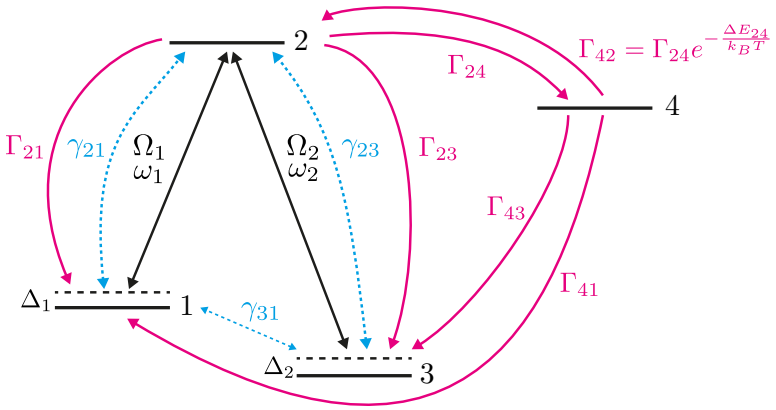

FIG. S10. Level scheme and corresponding transition rates employed for the optical Bloch equation model. The symbols are described in the text.

To model the dynamics of this open Λ type system we employ an optical Bloch equation model. Figure S10 displays a schematic representation of the modeled system. The Λ system is driven between the two ground states 1 and 3 and their common excited state 2. The rates occurring in the scheme are described in greater detail below. For the CPT measurements presented in the main text, state 1 equals $|2\rangle$ of the SiV$^-$ energy level scheme below 3.5 T and $|3\rangle$ above 3.5 T (as explained in section IV). State 2 equals $|D\rangle$ and state 3 equals $|1\rangle$ of the SiV$^-$ energy level scheme for all magnetic field values. This means that with one laser, we drive transition D1 for all values of the magnetic field. In the following, we name this the pump-transition because for the measurements presented here and we keep the corresponding laser fixed on resonance with this transition. With a second laser, we drive transition D2 below 3.5 T and transition D3 above 3.5 T. We name these transitions the probe-transitions as they are scanned with the laser frequency during the measurement. To derive the density matrix equations of motion, we start with the Hamiltonian $\mathcal{H}_{\text{int}}$ of the effective four-level system in the interaction picture, which, by applying the rotating-wave approximation, can be written as [9]

$$\mathcal{H}_{\text{int}} = \begin{bmatrix} 0 & \frac{\Omega_1}{2} & 0 & 0 \\ \frac{\Omega_1}{2} & \Delta_1 & \frac{\Omega_2}{2} & 0 \\ 0 & \frac{\Omega_2}{2} & \Delta_1 - \Delta_2 & 0 \\ 0 & 0 & 0 & 0 \end{bmatrix}, \tag{1}$$

with the pump (probe) laser Rabi frequency $\Omega_2 = \frac{\mu_{D1} E_2}{\hbar}$ ($\Omega_1 = \frac{\mu_{D2/3} E_1}{\hbar}$) on the transition D1 (D2 below 3.5 T, D3 above, as explained in section IV) and the corresponding laser detunings

$$\Delta_1 = \omega_{D2/3} - \omega_1 \tag{2a}$$
$$\Delta_2 = \omega_{D1} - \omega_2 \tag{2b}$$

for the probe and the pump transitions, respectively. With this Hamiltonian, the optical Bloch evolution equation can be written as

$$\frac{d\rho}{dt} = -\frac{i}{\hbar}[\mathcal{H}_{\text{int}}, \rho] + \mathcal{L}(\rho) + \mathcal{D}(\rho) + \mathcal{W}(\rho). \tag{3}$$

with the density matrix ρ and the Lindblad superoperator $\mathcal{L}(\rho)$ describing spontaneous emission processes. The matrix $\mathcal{D}(\rho)$ is used to describe additional dephasing processes and $\mathcal{W}(\rho)$ describes the coherence properties of the

lasers. Spontaneous emission processes are taken into account by coupling the SiV^- center to a reservoir into which photons can be emitted leading to a relaxation of the system. This is modeled using the Lindblad superoperator

$$\mathcal{L}(\rho) = \sum \mathcal{L}_{ij}(\rho) = -\frac{1}{2}\sum (C_{ij}^\dagger C_{ij}\rho + \rho C_{ij}^\dagger C_{ij}) + \sum C_{ij}\rho C_{ij}^\dagger \tag{4}$$

with the collapse operators

$$C_{ij} = \sqrt{\Gamma_{ij}}\,|j\rangle\langle i| \tag{5}$$

defining a relaxation from state $|i\rangle$ to state $|j\rangle$. With this, the matrix forms of the Lindblad operators $\mathcal{L}_{ij}$ for the individual decays from $|i\rangle$ to $|j\rangle$ of the system are given by

$$\mathcal{L}_{21}(\rho) = \begin{bmatrix} \Gamma_{21}\rho_{22} & -\frac{\Gamma_{21}}{2}\rho_{12} & 0 & 0 \\ -\frac{\Gamma_{21}}{2}\rho_{21} & -\Gamma_{21}\rho_{22} & -\frac{\Gamma_{21}}{2}\rho_{23} & -\frac{\Gamma_{21}}{2}\rho_{24} \\ 0 & -\frac{\Gamma_{21}}{2}\rho_{32} & 0 & 0 \\ 0 & -\frac{\Gamma_{21}}{2}\rho_{42} & 0 & 0 \end{bmatrix} \qquad \mathcal{L}_{23}(\rho) = \begin{bmatrix} 0 & -\frac{\Gamma_{23}}{2}\rho_{12} & 0 & 0 \\ -\frac{\Gamma_{23}}{2}\rho_{21} & -\Gamma_{23}\rho_{22} & -\frac{\Gamma_{23}}{2}\rho_{23} & -\frac{\Gamma_{23}}{2}\rho_{24} \\ 0 & -\frac{\Gamma_{23}}{2}\rho_{32} & \Gamma_{23}\rho_{22} & 0 \\ 0 & -\frac{\Gamma_{23}}{2}\rho_{42} & 0 & 0 \end{bmatrix}$$

$$\mathcal{L}_{24}(\rho) = \begin{bmatrix} 0 & -\frac{\Gamma_{24}}{2}\rho_{12} & 0 & 0 \\ -\frac{\Gamma_{24}}{2}\rho_{21} & -\Gamma_{24}\rho_{22} & -\frac{\Gamma_{24}}{2}\rho_{23} & -\frac{\Gamma_{24}}{2}\rho_{24} \\ 0 & -\frac{\Gamma_{24}}{2}\rho_{32} & 0 & 0 \\ 0 & -\frac{\Gamma_{24}}{2}\rho_{42} & 0 & \Gamma_{24}\rho_{22} \end{bmatrix} \qquad \mathcal{L}_{42}(\rho) = \begin{bmatrix} 0 & 0 & 0 & -\frac{\Gamma_{42}}{2}\rho_{14} \\ 0 & \Gamma_{42}\rho_{44} & 0 & -\frac{\Gamma_{42}}{2}\rho_{24} \\ 0 & 0 & 0 & -\frac{\Gamma_{42}}{2}\rho_{34} \\ -\frac{\Gamma_{42}}{2}\rho_{41} & -\frac{\Gamma_{42}}{2}\rho_{42} & -\frac{\Gamma_{42}}{2}\rho_{43} & -\Gamma_{42}\rho_{44} \end{bmatrix}$$

$$\mathcal{L}_{43}(\rho) = \begin{bmatrix} 0 & 0 & 0 & -\frac{\Gamma_{43}}{2}\rho_{14} \\ 0 & 0 & 0 & -\frac{\Gamma_{43}}{2}\rho_{24} \\ 0 & 0 & \Gamma_{43}\rho_{44} & -\frac{\Gamma_{43}}{2}\rho_{34} \\ -\frac{\Gamma_{43}}{2}\rho_{41} & -\frac{\Gamma_{43}}{2}\rho_{42} & -\frac{\Gamma_{43}}{2}\rho_{43} & -\Gamma_{43}\rho_{44} \end{bmatrix} \qquad \mathcal{L}_{41}(\rho) = \begin{bmatrix} \Gamma_{41}\rho_{44} & 0 & 0 & -\frac{\Gamma_{41}}{2}\rho_{14} \\ 0 & 0 & 0 & -\frac{\Gamma_{41}}{2}\rho_{24} \\ 0 & 0 & 0 & -\frac{\Gamma_{41}}{2}\rho_{34} \\ -\frac{\Gamma_{41}}{2}\rho_{41} & -\frac{\Gamma_{41}}{2}\rho_{42} & -\frac{\Gamma_{41}}{2}\rho_{43} & -\Gamma_{41}\rho_{44} \end{bmatrix}$$

with the transition rates Γ_{ij} and the density matrix elements ρ_{ij}. To account for additional pure dephasing processes (without transfer of population) between the two ground states as well as between the ground and excited states of the Λ system, we introduce the matrix

$$\mathcal{D}(\rho) = \begin{bmatrix} 0 & -\gamma_{21}\rho_{12} & -\gamma_{31}\rho_{13} & 0 \\ -\gamma_{21}\rho_{21} & 0 & -\gamma_{23}\rho_{23} & 0 \\ -\gamma_{31}\rho_{31} & -\gamma_{23}\rho_{32} & 0 & 0 \\ 0 & 0 & 0 & 0 \end{bmatrix} \tag{6}$$

acting on the off-diagonal density matrix elements, with γ_{ij} being the individual dephasing rates. Finally, the finite laser linewidths have to be taken into account as these additionally increase the dephasing rates of the states coupled to the laser light field. This effect is introduced into the model by the matrix

$$\mathcal{W}(\rho) = \begin{bmatrix} 0 & -\xi_1\rho_{12} & -\xi_{mut}\rho_{13} & 0 \\ -\xi_1\rho_{21} & 0 & -\xi_2\rho_{23} & 0 \\ -\xi_{mut}\rho_{31} & -\xi_2\rho_{32} & 0 & 0 \\ 0 & 0 & 0 & 0 \end{bmatrix} \tag{7}$$

with $\xi_{1,2}$ being the linewidths of the individual lasers and ξ_{mut} being the mutual coherence of the lasers.

To reduce the number of free parameters in the model, we use the following constraints:

- First, the Rabi frequencies of both transitions can be linked and Ω_2 can be expressed in terms of Ω_1 according to

$$\Omega_2 = \Omega_1 \cdot \sqrt{\frac{P_2}{P_1}} \cdot \frac{\mu_2}{\mu_1} \tag{8}$$

with the laser powers $P_{1,2}$ (proportional to the square of the laser light electric field amplitudes $E_{1,2}^2$) and the transition dipole moments μ_2 and μ_1 of the transitions involved as calculated from the group theoretical model presented in [4].

- Second, by comparing the measured spectrum of an SiV$^-$ center with its simulated counterpart calculated using a group-theoretical model presented in [4], it is possible to determine the relative transition dipole moments $\mu_{ij}^{x,y,z}$ of the individual optical transitions. With the resulting relative transition dipole moments, the individual transition rates Γ_{ij} can be linked to the total spontaneous decay rate Γ by the equation

$$\Gamma_{ij} = \frac{(\mu_{ij}^x + \mu_{ij}^y + \mu_{ij}^z)}{\sum(\mu_{ij}^x + \mu_{ij}^y + \mu_{ij}^z)}\Gamma \tag{9}$$

with the total spontaneous decay rate

$$\Gamma = \tau^{-1} \tag{10}$$

and τ being the lifetime of the SiV$^-$ center. Additionally, we assume thermalization between states 2 and 4 and therefore write $\Gamma_{42} = \Gamma_{24} e^{-\frac{\Delta E_{24}}{k_B T}}$, with ΔE_{24} being the mean energetic distance between the state $|D\rangle$ and the other excited states $|C\rangle$, $|B\rangle$ and $|A\rangle$ of the SiV$^-$ center.

- Finally, the two dephasing rates γ_{21} and γ_{23} are chosen such that they reproduce the total linewidth of the optical transition and are kept constant at these values (as these parameters do not affect the width of the CPT dip).

Using this approach, the only free parameters in the model are the Rabi frequency Ω_1 and the ground state dephasing rate γ_{31}. A single set of these parameters can be identified to model an experimentally observed CPT dip. We numerically solve the differential equations defined by Eq. 3 over the experimental integration time (ranging from 0.5 s to 8 s). A steady-state is reached within this time interval. We plot the normalized population of state $|4\rangle$ versus the two-photon detuning of the lasers. This population is directly proportional to the fluorescence of the A, B and C branches of optical transitions of the SiV$^-$ center as it results from the branching of $|D\rangle$ (state 2 in the model) into the other excited states of the SiV$^-$. For the measurement presented in Fig. 3(c) of the main text, the following set of transition and dephasing rates has been calculated from the model.

TABLE I. Transition and dephasing rates in angular frequency for the CPT measurement presented in Fig. 3(c) of the main text, determined from the optical Bloch equation model described above.

$\Gamma_{21} = 2\pi \cdot 3.0\,\text{MHz}$	$\Gamma_{23} = 2\pi \cdot 4.7\,\text{MHz}$
$\Gamma_{24} = 2\pi \cdot 88.1\,\text{MHz}$	$\Gamma_{42} = 2\pi \cdot 40.5\,\text{MHz}$
$\Gamma_{41} = 2\pi \cdot 19.3\,\text{MHz}$	$\Gamma_{43} = 2\pi \cdot 20.9\,\text{MHz}$
$\gamma_{21} = \gamma_{23} = 2\pi \cdot 3250\,\text{MHz}$	$\gamma_{31} = 2\pi \cdot 3.5\,\text{MHz}$

The minimum CPT dip width observed in this work amounts to 12.1 MHz in linear frequency [cf. Fig. 3(c) of the main text]. This width includes three main contributions, the ground state dephasing γ_{13}, the mutual coherence (here 5 MHz) of the two lasers and a power broadening described by the two Rabi frequencies of the lasers. By fitting the experimental data with this model, we could extract a value for $\gamma_{13} = 3.5 \pm 0.2$ MHz in linear frequency, corresponding to a T_2^* coherence time of 45 ns.

IV. MODELING OF THE CPT DIP WIDTH VARIATION

The eigenstates of the SiV$^-$ center, extracted from the group theoretical model described in [4], are of the form $|\Psi_{g/e}\rangle = \alpha|e_{g/e,+}\uparrow\rangle + \beta|e_{g/e,+}\downarrow\rangle + \gamma|e_{g/e,-}\uparrow\rangle + \delta|e_{g/e,-}\downarrow\rangle$, where α, β, γ and δ are complex numbers, $e_\pm$ refer to orbital components of the basis states and $\uparrow,\downarrow$ to their spin S_z component (the quantization axis being taken along the axis of the SiV$^-$ center). The subscripts g/e correspond to ground and excited states respectively. In order to extract the S_z component of the eigenstates of the SiV$^-$, one can make use of the projector $P = |\uparrow\rangle\langle\uparrow| + |\downarrow\rangle\langle\downarrow|$, which projects the eigenstate onto the spin subspace, thus one obtains

$$P|\Psi_{g/e}\rangle = (\alpha+\gamma)\,|\uparrow\rangle + (\beta+\delta)\,|\downarrow\rangle = c_\uparrow|\uparrow\rangle + c_\downarrow|\downarrow\rangle. \tag{11}$$

The coefficients $c_{\uparrow,\downarrow}$ refer to the ones introduced in Sec. II A. This can be rewritten in the form of $P|\Psi_{g/e}\rangle = \cos(\theta/2)\,|\uparrow\rangle + e^{i\phi}\sin(\theta/2)\,|\downarrow\rangle$ and represented as a vector on a Bloch sphere, where θ is the polar angle and ϕ the azimuthal angle. The Bloch vector of each eigenstate of the system varies with the magnetic field, especially at an anticrossing. In Fig. S11, we display them for different values of the magnetic field. The Bloch vectors of state $|1\rangle$ and $|2\rangle$ are antiparallel until state $|2\rangle$ undergoes an anticrossing with state $|3\rangle$. Above this anticrossing, states $|1\rangle$ and $|2\rangle$ have similar S_z components, and the Bloch vectors are not antiparallel any more. In contrast, states $|1\rangle$ and $|3\rangle$ now have opposite Bloch vectors. Therefore we choose to create the CPT dark state between states $|1\rangle$ and $|2\rangle$, below the anticrossing and between states $|1\rangle$ and $|3\rangle$ above the anticrossing [Fig. 4(a) of the main text].

As discussed in the main text of the paper, the external magnetic field introduces a static perturbation on the SiV^- electronic states. If the magnetic field is not applied parallel to the SiV^- high symmetry axis, then there is a competition between the internal quantization axis of the SiV^- center and the external axis defined by the magnetic field. As a result, the spin aligns with respect to an effective quantization axis. The direction of this effective axis depends on the ratio of the magnetic field interaction (Zeeman interaction) and the SiV^- orbital interactions (spin-orbit coupling and Jahn-Teller effect). For a given magnetic field value, it is therefore possible to apply a basis transformation to the spin states in order to represent them along the effective quantization axis. In the Bloch vector representation (Fig. S11), this transformation corresponds to a rotation of the vectors, such that they are aligned along the poles of the Bloch sphere. This can be seen for states $|1\rangle$ and $|2\rangle$ at $B = 1\,\mathrm{T}$, which after a suitable rotation would be aligned antiparallel pointing to the north- and south pole of the Bloch sphere, respectively.

In Ref. [10], an individual Zeeman sublevel in the excited state manifold of the SiV^- was resonantly populated. An orbital relaxation takes place within the lifetime of the excited states, which is generally of the order of $1 - 4\,\mathrm{ns}$ [11]. It was demonstrated that this relaxation is spin-selective, as fluorescence spectra show that levels with opposite spin to the addressed one do not get populated. The spin component of a state can thus prevent population transfer to a state of opposite spin.

In order to understand the variation of the CPT dip width as a function of the magnetic field (presented in Fig. 4 (b) of the main text), we introduce a simple model. In this model we calculate the evolution of the spin overlap between the two ground states used for CPT, based on the model in [4]. To do so, we consider the squared scalar product, e.g. $\left|\langle\Psi_1|P^\dagger P|\Psi_2\rangle\right|^2$, of the spin projections of the two states. This quantity is multiplied by a Boltzmann factor $\mathrm{e}^{-\Delta E/k_B T}$ to take into account the phonon population most likely involved in the orbital relaxation. In this factor, $\Delta E = E(\Psi_1) - E(\Psi_2)$ is the energy difference between the states $\Psi_{1,2}$ used for CPT, $T = 4\,\mathrm{K}$ is the temperature and k_B is the Boltzmann constant.

The product of spin overlap and Boltzmann factor is then compared to the experimental CPT dip line widths [Fig. 4(b) of the main text] as a function of magnetic field B, keeping two free parameters which are a scaling factor b and an offset a, i.e. we use the fitting function

$$f(B) = a + b \cdot \left|\langle\Psi_1|P^\dagger P|\Psi_2\rangle\right|^2 \mathrm{e}^{-\Delta E/k_B T}. \tag{12}$$

The offset a embodies the contributions to the CPT linewidth from power broadening due to the two excitation lasers, the mutual coherence of the two lasers (5 MHz in our case), as well as further decoherence of the spin state due to the influence of the environment such as neighboring spins (NV^- centers, P1 centers,...). The good agreement between this simple model and the data confirms the importance of the spin component in the coherence of the state of the SiV^- center. In the vicinity of the anticrossing, the spin projection of state $|2\rangle$ changes sign, thus increasing its overlap with state $|1\rangle$. Consequently, relaxation between $|1\rangle$ and $|2\rangle$ becomes possible, thus reducing the lifetime of the dark state. At the same time, the spin projection of $|3\rangle$ becomes opposite to that of $|1\rangle$, allowing to observe a dark state between those two states. The relaxation of the energy levels forming the dark state to other levels is not taken into account in this model. The contribution of phonons to the decoherence is here highly simplified and temperature-dependent measurements will allow to identify the exact mechanism involved and thus refine the model presented in this section.

[1] J. F. Ziegler, M. D. Ziegler, and J. P. Biersack, Nuclear Instruments and Methods in Physics Research, Section B: Beam Interactions with Materials and Atoms **268**, 1818 (2010).

[2] E. Neu, M. Agio, and C. Becher, Optics Express **20**, 19956 (2012).

[3] J. Riedrich-Möller, L. Kipfstuhl, C. Hepp, E. Neu, C. Pauly, F. Mücklich, A. Baur, M. Wandt, S. Wolff, M. Fischer, S. Gsell, M. Schreck, and C. Becher, Nature Nanotechnology **7**, 69 (2012).

[4] C. Hepp, T. Müller, V. Waselowski, J. N. Becker, B. Pingault, H. Sternschulte, D. Steinmüller-Nethl, A. Gali, J. R. Maze, M. Atatüre, and C. Becher, Physical Review Letters **112**, 036405 (2014).

[5] A. M. Zaitsev, *Optical Properties of Diamond: A Data Handbook* (Springer-Verlag, Berlin, 2001).

[6] F. Jelezko, T. Gaebel, I. Popa, M. Domhan, A. Gruber, and J. Wrachtrup, Phys. Rev. Lett. **93**, 130501 (2004).
[7] C. D. Clark, H. Kanda, I. Kiflawi, and G. Sittas, Phys. Rev. B **51**, 16681 (1995).
[8] S. Zaske, A. Lenhard, C. A. Keßler, J. Kettler, C. Hepp, C. Arend, R. Albrecht, W. M. Schulz, M. Jetter, P. Michler, and C. Becher, Physical Review Letters **109** (2012).
[9] A. Lazoudis, T. Kirova, E. H. Ahmed, L. Li, J. Qi, and A. M. Lyyra, Physical Review A **82**, 023812 (2010).
[10] T. Müller, C. Hepp, B. Pingault, E. Neu, S. Gsell, M. Schreck, C. Becher, and M. Atatüre, Nature Communications **5**, 3328 (2014).
[11] H. Sternschulte, K. Thonke, R. Sauer, P. C. Münzinger, and P. Michler, Physical Review B **50**, 14554 (1994).

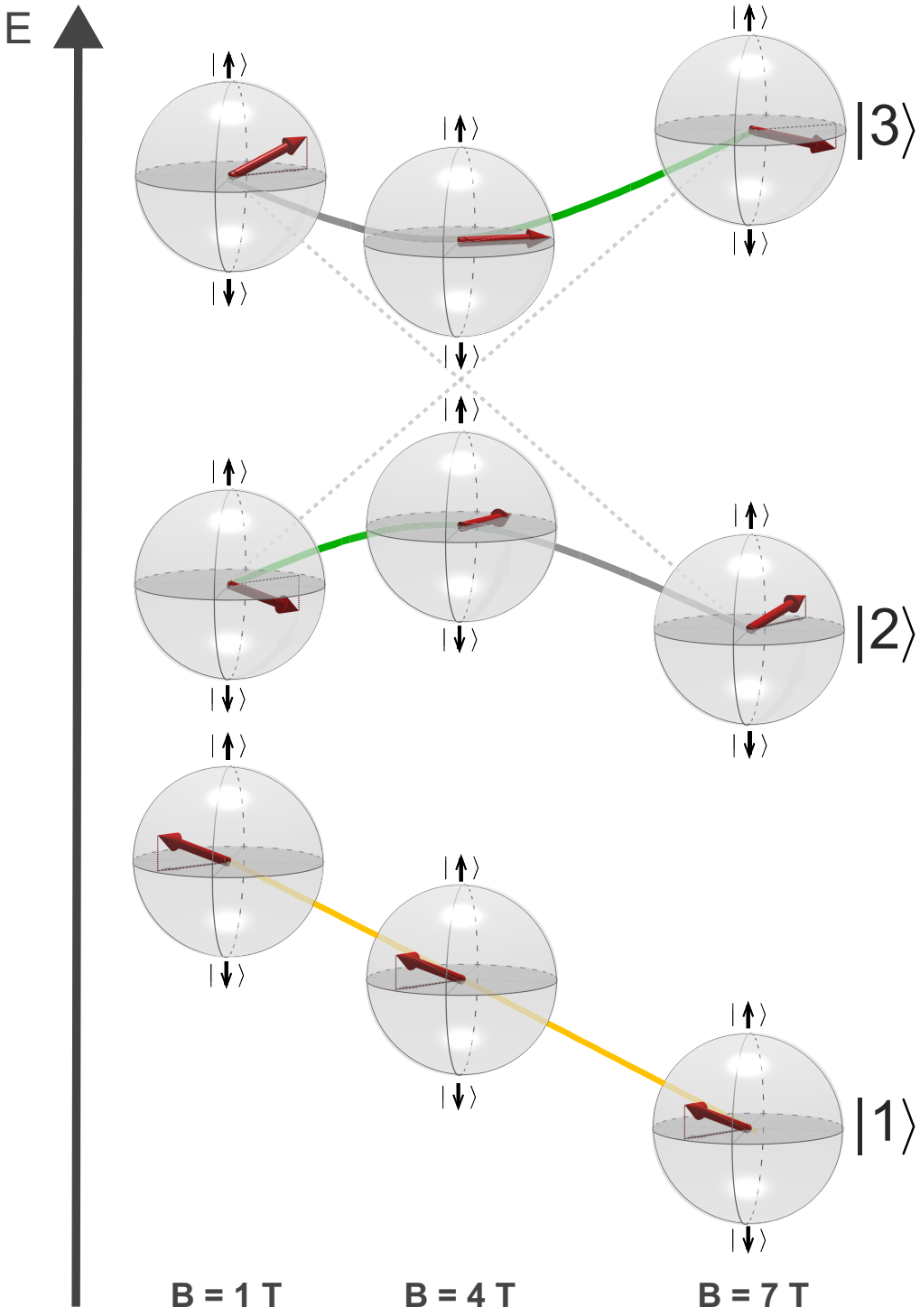

FIG. S11. Bloch-sphere representation of the states $|1\rangle$, $|2\rangle$ and $|3\rangle$ at 1 T, 4 T and 7 T.